JACS
JOURNAL OF THE AMERICAN CHEMICAL SOCIETY

ARTICLE

pubs.acs.org/JACS

Formation of Heterodimer Nanocrystals: UO_2/In_2O_3 and $FePt/In_2O_3$

Huimeng Wu, Ou Chen, Jiaqi Zhuang, Jared Lynch, Derek LaMontagne, Yasutaka Nagaoka, and Y. Charles Cao*

Department of Chemistry, University of Florida, Gainesville, Florida 32611, United States

Supporting Information

ABSTRACT: This Article reports a mechanistic study on the formation of colloidal UO_2/In_2O_3 and $FePt/In_2O_3$ heterodimer nanocrystals. These dimer nanocrystals were synthesized via the growth of In_2O_3 as the epitaxial material onto the seed nanocrystals of UO_2 or FePt. The resulting dimer nanocrystals were characterized using X-ray powder diffraction (XRD), energy dispersion spectroscopy, transmission electron microscopy (TEM), scanning transmission electron microscopy, and high-resolution TEM (HRTEM). The results from XRD and HRTEM clearly show that lattice strains exist in both of these dimer nanocrystals. Interestingly, the lattice of In_2O_3 expands in UO_2/In_2O_3 dimers, whereas $FePt/In_2O_3$ dimers exhibit compressed In_2O_3 lattices. Using HRTEM and nanocrystal structure simulations, we have identified the crystallographic orientation of the attachment of the two segments in these two types of dimers. An unconventional Miller index was introduced to describe the crystallographic orientation of these heterodimer nanocrystals. On the basis of the results herein as well as those from other researchers, we propose an empirical law for the determination of the crystallographic attachment orientation in heterodimers: instead of growth on the facet of the seed nanocrystals where lattice mismatch is minimized, the growth of an epitaxial material often chooses the crystal facets where the first atomic monolayer of this material has the strongest affinity for the seed nanocrystals.

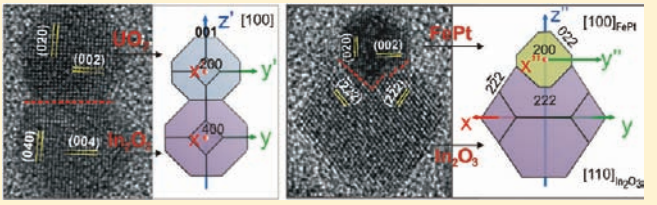

INTRODUCTION

The ability to synthesize hybrid nanocrystals with a spatially anisotropic distribution of their material domain components opens up new opportunities for tailoring the physical and chemical properties of nanostructures[1−9] and provides a new class of building blocks for applications ranging from biomedical diagnosis to solar energy conversion.[10−13] These hybrid nanocrystals include linear and/or branched CdX nanocrystals (X = S, Se, Te) that have one or more heterojunctions,[10] nanodumbbells composed of semiconductors and metals or binary semiconductors,[4,11,12,14−18] and a variety of asymmetric nanocrystal dimers, trimers, and oligomers of binary or ternary compositions, such as semiconductors, metals, and metal oxides.[19−25] These hybrid nanocrystals possess two or more distinct quantum dots and/or rods connected epitaxially at heterojunctions within single nanocrystals. Such nanostructures allow for the coupling of quantum dots and rods through defined potential barriers arranged in a three-dimensional (3D) space at well-defined angles and distances, which subsequently manipulates the wave functions and spins of carriers, plasmon resonances, and other material properties.[10,26,27]

In addition, the asymmetric coupling of two semiconductors or a semiconductor and a metal allows directional charge separation at their junction, which is important for devices such as solar cells and LEDs and can also introduce new photocatalytic properties.[1,10,28−30] Hybrid nanocrystals that incorporate a magnetic segment frequently exhibit novel magnetic behavior substantially diverging from that of the corresponding isolated magnetic nanocrystals.[9,31] With heterogeneous junctions, these nanocrystals can display combined multiple functions, such as magnetic−fluorescent nanoparticles, which are useful in biological separation and tracking.[32] Moreover, unlike their isotropic counterparts, these anisotropic nanocrystals often exhibit multiple distinct surface chemistry properties. This unique surface functionality can introduce new catalytic properties[21] and can also allow for selective surface functionalization of each anisotropic nanocrystal at a well-defined 3D geometry, which has important implications for nanocrystal assembly and biomedical applications.[25]

To date, a number of colloidal methods have been developed for the synthesis of anisotropic hybrid nanocrystals.[4,10−12,14−25,33] Most of these methods are based on a seed-growth mechanism, in which an "epitaxial (EP) material" grows onto the nanocrystal seeds of a "substrate material" in solution.[22,33−36] These seed particles are either premade or made in situ with the growth of EP materials in a one-pot synthesis;[2,37] they can be spheres, linear rods, or branched tetrapods.[10,11,14,38−40] The growth of EP materials can be triggered either thermally or photochemically.[41,42] The formation of hybrid nanocrystals is primarily affected by the following parameters of the substrate and EP materials: crystal structure, lattice constant, and the nature of the chemical bonds.

If these parameters are very close between the substrate and EP materials, anisotropic hybrid nanocrystals form when the seed nanocrystals are capped with strong facet-selective-adhering

Received: March 15, 2011
Published: August 09, 2011

ligands[39,40,43,44] and/or the growth of EP materials undergo kinetically driven processes.[45,46] When one or more of these intrinsic parameters substantially differs in the two materials, the formation of anisotropic hybrid nanocrystals is often expected. Examples include heterogeneous dimers, trimers, or oligomers of CdS(Se)/Au,[11,15,47,48] FePt/CdS(Se),[4,37] FePt/Fe_3O_4,[2] FePt/PdS(Se),[49] Fe_3O_4/CdS,[32,37] Au/Fe_3O_4,[19] Au/PbS(Te), PbS(Se)/Au/Fe_3O_4, CdS(Se)/PbSe,[17] CdSe/Co,[50] TiO_2/Co,[40] TiO_2/ZnO,[38] TiO_2/γ-Fe_2O_3,[33,37] Au/$CoPt_3$,[45] and Au/Co (Te).[39,51,52]

Despite this progress, a full understanding of the formation mechanisms behind anisotropic hybrid nanocrystals is still lacking. It still remains a challenge for the rational design and synthesis of colloidal anisotropic hybrid nanocrystals with prechosen compositions in controlled heterogeneous attachment geometry. To overcome this difficulty, one needs to answer the following fundamental questions: (1) What are the general criteria for choosing colloidal synthesis parameters for making hybrid anisotropic nanocrystals? (2) What are the general rules for the epitaxial attachment of an EP material to the seeds of the first material?

To answer these fundamental questions, we herein used UO_2 and FePt nanocrystals as two model seed systems to study the formation of colloidal hybrid heterodimers with the epitaxial growth of an identical EP material: In_2O_3. These two seed crystals have identical space group symmetry ($Fm\bar{3}m$), but their lattice constants and the nature of their chemical bonds differ significantly. UO_2 has a fluorite structure with uranium cations occupying the positions of the calcium cations and oxygen anions occupying the positions of the fluoride anions. FePt crystals have an alloy structure with Fe and Pt occupying equivalent lattice points in a face-centered cubic (fcc) unit cell.[53] The In_2O_3 made herein has a bixbyite crystal structure with a space group $Ia3$. The unit cell of In_2O_3 is large and contains 80 atoms, and it is related to the fluorite structure, from which it can be derived by removing one-quarter of the anions.[54]

In addition, UO_2 is a highly efficient and stable catalyst for the destruction of chlorine-containing organic pollutants at moderate temperatures, and it is also a material with a high Seebeck coefficient, which could be important to thermopower applications.[55] FePt nanocrystals can be used as electrocatalysts.[48] FePt nanocrystals with an fcc structure are superparamagnetic at room temperature.[56,57] After thermal annealing, fcc FePt can be converted into face-centered tetragonal (fct) nanostructures with coercivities as high as 30 kOe,[58] which is important to applications such as high density data storage and high performance permanent magnets.[57] In_2O_3 has been widely used for ultrasensitive toxic gas detectors,[59−61] transparent conductors,[62] solar cells, and optoelectronic devices.[63] The anisotropic nanocrystals of these materials are expected to exhibit interesting and unique catalytic and magnetic properties. We herein focus on a mechanistic study of how these materials form heterogeneous epitaxial junctions.

In this study, a two-step synthesis was used to make anisotropic hybrid nanocrystals: first, spherical UO_2 nanocrystal seeds and FePt nanoprism seeds were synthesized, and then In_2O_3 was grown upon the seeds, forming hybrid dimer nanocrystals. We expect that the shape difference in these two types of seed nanocrystals can provide additional hints on the formation mechanism of heterogeneous junctions between In_2O_3 and the seeds. The resulting UO_2/In_2O_3 and FePt/In_2O_3 heterodimer nanocrystals were characterized using a transmission electron microscope (TEM), energy-dispersive X-ray spectroscopy (EDS), X-ray diffraction (XRD), and high-resolution TEM (HRTEM). Results from these structural characterizations show that the epitaxial attachment of In_2O_3 onto either seed is not at a random orientation, but through specific crystal facets depending on the structure parameters of the seed nanocrystals.

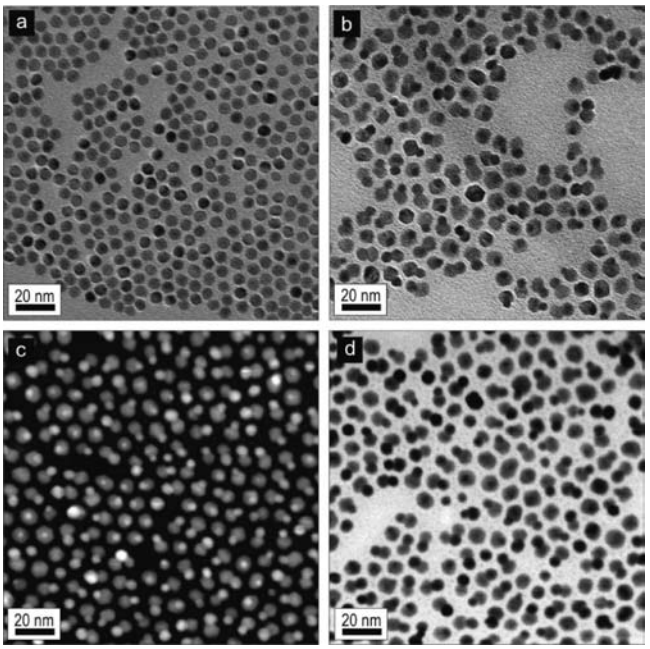

Figure 1. TEM images of (a) a monolayer of UO_2 seeds; the size is 6.2 ± 0.2 nm in diameter. (b) UO_2/In_2O_3 hybrid nanocrystals. (c) A dark-field STEM image of UO_2/In_2O_3 hybrid nanocrystals and (d) a bright-field STEM image of hybrid nanocrystals. The size of UO_2/In_2O_3 dimers is 5.7 ± 0.5 nm UO_2 and 7.7 ± 0.6 nm In_2O_3.

In the following sections, we shall present and discuss our experimental results on the synthesis and characterization of the UO_2/In_2O_3 and FePt/In_2O_3 nanocrystals. We then shall make some general remarks on the formation of heterogeneous nanocrystals and give new insights into the mechanisms for the orientation of the crystallographic attachment of two materials in heterogeneous nanocrystals.

RESULTS AND DISCUSSION

Synthesis of Heterodimer Nanocrystals. We used a two-step synthesis for making heterodimer nanocrystals: (1) synthesis of nanocrystal seeds of a substrate material; and (2) growth of an EP material on the seeds. UO_2 nanocrystal seeds were synthesized by thermal decomposition of uranyl acetylacetonate in a mixture of oleic acid, oleylamine, and 1-octadecene (ODE).[73] The final size of UO_2 nanocrystals in this synthesis can be easily tuned by varying the amount of oleic acid and oleylamine. Here, we chose UO_2 nanocrystals of 6.2 nm in diameter as seeds for In_2O_3 growth (Figure 1a). The In_2O_3 growth stock solution was prepared according to a literature method.[59]

Typically, unpurified 6.2 nm UO_2 nanocrystal solution was diluted with ODE and heated to 300 °C, followed by the injection of the indium oxide precursor into the reaction solution at 300 °C (for details, please see the experimental part in the Supporting Information). TEM shows that the resulting heterodimer nanocrystals have a darker segment (i.e., UO_2) of ~5.7 nm

and a lighter segment (i.e., In_2O_3) of ~7.7 nm (Figure 1b). The reduced size of UO_2 segments in the heterodimers is due in part to the etching of the original UO_2 nanocrystals by oleic acid and oleylamine in ODE. In addition, EDS analysis shows that the resulting dimer nanocrystals have a U/In ratio of ~0.29, which is very close to the U/In ratio (~0.30) calculated using the dimensions of the dimer nanocrystals determined by TEM measurements (Figure 1b). The percentage of dimers, trimers, and individual nanocrystals was determined by counting more than 300 nanocrystals. The results show ~92% dimers, ~3% trimers, and ~5% individual UO_2 (it should be noted that the final nanocrystals were purified with size-selection precipitation).

These UO_2/In_2O_3 heterodimer nanocrystals were further characterized using scanning TEM (STEM) in the modes of high-angle annular dark field (HAADF) and bright field (Figure 1c and d). The HAADF detector of a STEM collects all of the electrons that have been scattered at high angles to form a *Z*-contrast image on composition through the Z^2 dependence of the scattering cross section.[64] Uranium atoms possess a much larger scattering cross-section than do indium atoms; thus the UO_2 component appears as white dots, whereas the In_2O_3 component appears as darker dots in the HAADF image (Figure 1c). In contrast, the bright field detector collects the transmitted beam, the electrons that passed through the sample without being scattered. Therefore, bright field STEM can provide a complementary image to the HAADF image of UO_2/In_2O_3 heterodimers: the UO_2 component appears as darker dots, whereas the In_2O_3 component appears as lighter dots (Figure 1d).

Further mechanistic studies show that a successful synthesis of UO_2/In_2O_3 heterodimers requires prevention of new nucleation of the In_2O_3 nanocrystals in the In_2O_3 growth step. When we used 320 °C as the reaction temperature for In_2O_3 growth, we found that this reaction temperature does not significantly affect the size of UO_2 nanocrystal seeds in growth solution. UO_2 seeds were reduced to 5.9 nm with a size distribution of 7%, which is nearly identical to that of those UO_2 particles in the reaction at 300 °C. After an injection of indium oxide precursor solution into the UO_2 seed solution at this growth temperature (320 °C), however, significant nucleation of In_2O_3 nanocrystals took place. The formation of UO_2/In_2O_3 heterodimers was not observed, and only two types of particles were found in the final reaction mixture: spherical UO_2 nanocrystals of 4.5 nm in diameter and octahedral In_2O_3 nanocrystals of 8.2 nm in edge length (Figure S1 in the Supporting Information). Interestingly, the size distributions of these two types of nanocrystals are fairly narrow (relative standard deviations are less than 7%).

To further study the mechanism of heterodimer formation, we used FePt rectangular nanoprisms as seeds for growing indium oxide. FePt nanocrystals and UO_2 nanocrystals possess the same space group (i.e., $Fm\bar{3}m$, fcc) (UO_2, PDF#41-1422; FePt, PDF#29-0717), but they exhibit dramatic differences in their lattice constants and in the nature of their chemical bonds. An FePt crystal has a lattice constant of 0.3813 nm, and it is formed through metallic bonds of the Fe and Pt atoms that occupy equivalent lattice points in the fcc unit cell. The lattice constant of UO_2 crystals is 0.5467 nm, and the crystal is formed through ionic bonds between uranium and oxygen. The structure of UO_2 can be viewed as an fcc lattice of uranium cations ($Z = 4$), with the oxygen anions occupying all of the tetrahedron holes ($Z = 8$). The tetrahedron cavities reside on a simple cubic lattice, which is one-half the dimension of the uranium fcc lattice. In addition to these differences between the UO_2 and FePt seeds, the shape of

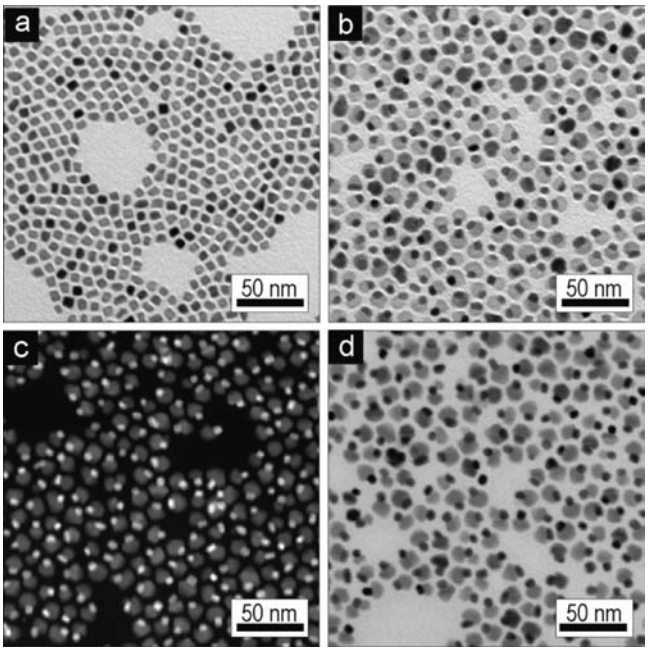

Figure 2. Typical TEM images of (a) FePt seeds taken from a typical synthesis solution at 300 °C and (b) FePt/In_2O_3 heterodimers. (c) A dark-field STEM image and (d) a bright-field STEM image of FePt/In_2O_3 hybrid nanocrystals.

FePt nanocrystal seeds would provide further hints to the detailed mechanism of heterodimer formation.

FePt rectangular nanoprisms were synthesized using a modified method based on the one developed by Sun et al.[53,57] The synthesis was carried out at 205 °C, and FePt nanocubes were obtained in Sun's method. However, the modified method herein resulted in FePt nanocrystals, of which more than 90% are rectangular prisms with dimensions of 5.5 × 5.5 × 6.5 nm. Under TEM, these nanoprisms appear as squares (5.5 × 5.5 nm) or rectangles (5.5 × 6.5 nm) depending on their orientation (Figures 2a and S1a in the Supporting Information). Typical HRTEM images of both single squares and rectangles show square lattice cross-fringes with an identical interfringe distance of 0.19 nm, which is close to the (200) *d*-spacing in the fcc FePt crystals (Figure S2b and S2d). Fast Fourier transformation (FFT) of the HRTEM image further reveals the two 4-fold symmetry of (200) and (220) faces of the fcc lattice along the [001] zone axis (Figure S2c and S2e in the Supporting Information). All together, these data suggest that FePt rectangular nanoprisms are closed by six {100} faces of the FePt fcc crystals. In addition, an in situ EDS analysis shows that the resulting FePt nanoprisms have a Fe/Pt ratio of nearly 1:1.

FePt/In_2O_3 heterodimer nanocrystals were synthesized according to a similar protocol for UO_2/In_2O_3 synthesis. We used the unpurified FePt nanocrystals as seeds (Figure 2a) and 300 °C as the growth temperature for the growth of In_2O_3. The resulting heterodimer nanocrystals possess a darker segment (i.e., FePt) and a lighter segment (i.e., In_2O_3, Figure 2b). The edges of the FePt seeds were truncated after the formation of dimers, and the average volume of the FePt components in the dimers decreases approximately 30% as compared to that of the FePt seeds. The In_2O_3 components in the dimers appear as octahedrons with an edge length of 10.1 ± 0.6 nm and a diagonal length of 14.1 ± 0.7 nm. The HAADF and bright field STEM images further

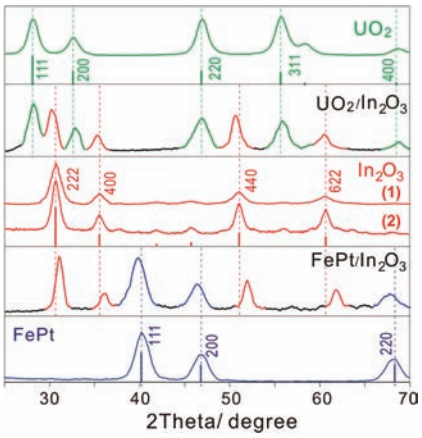

Figure 3. XRD spectra of UO_2/In_2O_3 and $FePt/In_2O_3$ hybrid heterodimers. The PDF no. 41-1422, PDF no. 06-0416, and PDF no. 29-0717 data are shown in green (UO_2), red (In_2O_3), and blue (FePt) lines. The individual UO_2 and FePt nanocrystals prior to In_2O_3 growth as well as independently synthesized In_2O_3 nanocrystals with diameter of 7 nm (1) and 11 nm (2) are shown in green (UO_2), red (In_2O_3), and blue (FePt) spectra.

reveal the contrast of the FePt and In_2O_3 segments in these dimers (Figure 2c and d). In addition, an in situ EDS analysis shows that the Fe/Pt ratio is about 1:1, nearly identical to that of FePt seeds. The Pt/In ratio is 1:6.7, which is consistent with the dimer dimensions determined using TEM.

XRD Analysis of Heterodimer Nanocrystals. A powder XRD pattern of a typical sample of UO_2/In_2O_3 heterodimers (as shown in Figure 1b−d) exhibits nine Bragg reflection peaks arising from both UO_2 and In_2O_3 (Figure 3). These peaks are broadened because of the finite crystalline domain size of UO_2/In_2O_3 heterodimers. The UO_2 peaks are composed of characteristic Bragg reflections of the {111}, {200}, {220}, {311}, and {400} fcc crystal facets, whereas the In_2O_3 peaks are from the {222}, {400}, {440}, and {622} reflections of a bixbyite crystal structure (Figure 3).

As compared to their counterparts in bulk (PDF no. 41-1422, PDF no. 06-0416), as well as in isolated nanocrystals, the UO_2 peaks shift slightly toward higher angles, whereas In_2O_3 peaks shift toward lower angles (Figure 3 and Table S1 in the Supporting Information). These XRD data indicate that the UO_2 lattice is compressed and In_2O_3 lattice is expanded in UO_2/In_2O_3 heterodimers. These structural changes in UO_2 and In_2O_3 are attributed to the lattice strain introduced by the epitaxial growth of In_2O_3 onto UO_2 seeds. With this lattice strain configuration, the In_2O_3 epitaxial layers should have a smaller *d*-spacing than that of the UO_2 substrate layers at the UO_2/In_2O_3 heterojunction. In addition, the compression of the UO_2 lattice and the expansion of the In_2O_3 lattice are not identical among different crystal facets (Table S1 in the Supporting Information). This result suggests that the In_2O_3 growth induced lattice strain is not homogeneous in UO_2/In_2O_3 heterodimers.

The XRD analysis shows that the $FePt/In_2O_3$ heterodimers (shown in Figure 2) also exhibit the lattice compression or expansion of their two segments (Figure 3). A typical powder XRD pattern of the $FePt/In_2O_3$ heterodimers consists of seven characteristic peaks from an fcc FePt and a bixbyite In_2O_3 crystal: the {111}, {200}, and {220} peaks of FePt, and the {222}, {400}, {440}, and {622} peaks of In_2O_3 (Figure 3). In comparison with their bulk counterparts (PDF no. 29-0717 and PDF no. 06-0416) and isolated FePt nanocrystals, the FePt peaks shift to lower angles with an average expansion of lattice constant of ~2.5%, whereas the In_2O_3 peaks shift to higher angles with an average compression of ~1.7% (Table S1). The expansion of FePt and the compression of In_2O_3 are nearly identical among the Bragg peaks of these $FePt/In_2O_3$ dimers (Table S1).

These structural changes in FePt and In_2O_3 are also attributed to the lattice strain introduced by the epitaxial growth of In_2O_3 onto FePt seeds. In this case, the In_2O_3 should grow along a crystallographic orientation, in which the lattice constant of the In_2O_3 epitaxial layer is larger than that of the FePt substrate layers. In addition, these $FePt/In_2O_3$ dimers exhibit the compression of In_2O_3 lattice, demonstrating an interesting example in contrast with those UO_2/In_2O_3 dimers, which exhibit the expansion of In_2O_3 lattice (Figure 3).

Beside the lattice strain effect assigned above, alloying or doping could also lead to lattice compression or expansion. This assumption could explain the lattice changes of In_2O_3. For example, the lattice of In_2O_3 could expand due to doping with uranium during the growth of UO_2/In_2O_3 dimers; doping with Fe during the growth of $FePt/In_2O_3$ dimers could cause the compression of In_2O_3 lattice. However, this assumption cannot explain the lattice compression or expansion of the nanocrystal seeds, because it is unlikely that these UO_2 or FePt seed nanocrystals get doped with (or alloyed with) indium ions (or atoms) during the growth of In_2O_3 under the current synthesis conditions.

Although XRD is a well-established technique for the characterization of lattice strains in heterogeneous thin films,[65] only a few reports show that lattice strains in colloidal heterogeneous nanocrystals can be clearly revealed by XRD analysis.[66] This difficulty likely arises from the following reasons. First, the nanometer-scale crystalline domain of nanocrystals broadens their XRD peaks, making it difficult to identify the small changes in their peak positions.

Second, the randomly oriented heterogeneous nanocrystals could result in XRD peaks at positions with an average effect of the lattice compression and expansion. Powder XRD measures ensemble samples of colloidal nanocrystals, which are often randomly aligned on substrates. The epitaxial growth often leads to lattice strain in the epitaxial crystal planes, while having an opposite effect in those planes parallel to the growth direction because of the Poisson effect.[67,68] In other words, epitaxial growth could lead to both lattice expansion and compression for the same materials at different crystal orientations, but the ratio of the lattice expression and compression is different due to the Poisson ratios of these materials.[67] Therefore, randomly oriented heterogeneous nanocrystals often give rise to lattice strain-induced XRD peak broadening instead of peak shifting.

Third, some heterogeneous nanocrystals could relax their lattice strains locally at the heterojunction interface through crystal defects such as point defects and dislocations. Fourth, the sample quality could also play a major role. Because of the difficulty in controlling the kinetics in the syntheses for making heterogeneous nanocrystals, the products of these syntheses are often composed of a substantial amount of seed nanocrystals (e.g., UO_2, FePt) and nanocrystals made of EP materials (e.g., In_2O_3), which could lead to significant interference in the identification of lattice strain using XRD. Therefore, our observation of lattice strains in the UO_2/In_2O_3 and $FePt/In_2O_3$ dimers should be due to their unique intrinsic material characteristics as well as the high purity of the dimer samples.

HRTEM and Nanocrystal Structure Simulations. On the basis of a combination of HRTEM and nanocrystal structure

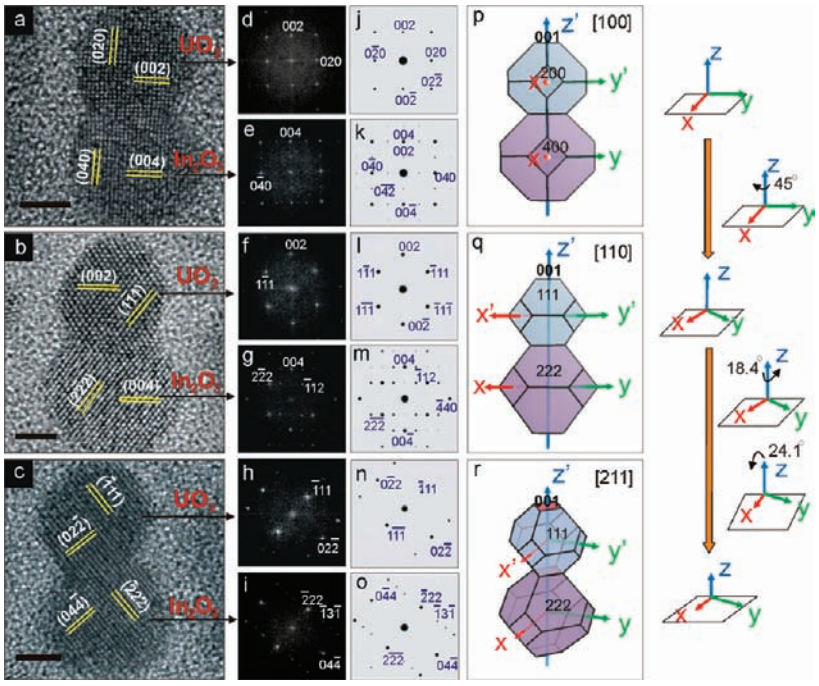

Figure 4. (a−c) HRTEM images of UO_2/In_2O_3 hybrid nanocrystals at different orientations. Fast Fourier transform (FFT) patterns of the HRTEM images are shown in (d)−(i). The simulated electron diffraction patterns of [110]-, [100]-, and [211]-oriented UO_2/In_2O_3 hybrid nanocrystals are shown in (j)−(o). Cartoons of UO_2/In_2O_3 hybrid nanocrystals at different orientations are shown in (p)−(r). The scale bars are 3 nm.

simulation, we studied the 3D structure of the heterojunction interface in these dimers. Our HRTEM observations show that UO_2/In_2O_3 dimers exhibit three typical types of cross-fringe images, which allow us to unambiguously identify that the UO_2 and In_2O_3 segments possess the same zone axis of a cubic crystal structure (Figure 4a−c). The TEM image viewed along the [100] zone shows the {002} fringes of the UO_2 segment and the {004} fringes of the In_2O_3 segment. Viewed along the [110] zone axis, the UO_2 segment exhibits the {111} and {002} fringes of an fcc structure, and the In_2O_3 segment shows the {222} and {004} fringes of a bixbyite crystal structure (Figure 4b). On the [211] zone, the UO_2 segment exhibits the {111} and {022} fringes, and the In_2O_3 segment shows the {222} and {044} fringes (Figure 4c). In addition, these lattice fringe assignments are further confirmed by the fast Fourier transform (FFT) images of corresponding HRTEM images (Figure 4d−i).

Moreover, in these HRTEM images, the fringes of the {111}, {002}, and {022} of UO_2 segments are parallel to their corresponding counterparts in the In_2O_3 segments: the {222}, {004}, and {044} fringes (Figure 4a−c). This result shows that all three crystal axes of the fcc UO_2 segment should be parallel to those of the cubic bixbyite In_2O_3 segment in dimer nanocrystals, which corresponds to the following epitaxial relationships: UO_2 (020)‖ In_2O_3 (040) as shown in the [100] zone image, UO_2 $(1\bar{1}1)$‖ In_2O_3 $(2\bar{2}2)$ and UO_2 $(1\bar{1}\bar{1})$‖ In_2O_3 $(2\bar{2}\bar{2})$ in the [110] zone image, and UO_2 $(11\bar{1})$‖ In_2O_3 $(22\bar{2})$ and UO_2 $(2\bar{2}0)$‖ In_2O_3 $(4\bar{4}0)$ in the [211] zone image. The fringes are visible across the heterojunction and through entire nanocrystals in accordance with the epitaxial growth of the In_2O_3 in these dimer particles.

A critical question arises over whether these nanocrystals have the same In_2O_3 epitaxial growth direction and heterojunction interface. According to the statistical data from HRTEM observations, in the dimers with cross-fringe images, ~65% exhibit [110] zone image, ~30% have [100] zone image, and ~5% of them exhibit [211] zone image. To determine the relationship between these three types of images as well as the In_2O_3 epitaxial growth direction and heterojunction interface in these heterodimers, we used Crystalmaker software (version 2.1.2) to conduct a simulation of the heterodimer nanocrystal structures.

First, 5.7 nm UO_2 and 10.6 nm In_2O_3 octahedron nanocrystals were constructed. Second, the two 3D nanocrystal models were orientated to the [100] zone direction using their simulated electron diffraction patterns as an indicator, and then the two nanocrystal models were attached together along their *z*-axis, resulting in a UO_2/In_2O_3 dimer model with the *x*- and *y*-axes of the UO_2 and In_2O_3 segments parallel to each other (Figure 4p). The simulated electron diffraction (ED) patterns of the UO_2 and In_2O_3 segments in this dimer model perfectly match the FFT images of the UO_2 and In_2O_3 segments in the [100] zone HRTEM image (Figure 4j,k,d,e). It is worth noting that this dimer attachment orientation is unique according to our simulation.

When rotated 45° along its *z*-axis, the dimer model exhibits simulated ED patterns of its two segments in perfect agreement with the FFT images of the [110] HRTEM image (Figure 4f,g,l,n). The dimer model also exhibits simulated ED patterns consistent with the FFT images of the [211] image when it was rotated 18.4° along its *z*-axis and then the *z*-axis is tilted at 24.1° out of the substrate plane (Figure 4). Taken together, these results suggest that the crystal lattices of the UO_2 and In_2O_3 segments are indeed oriented relative to each other in the same way in these three types of images. These UO_2/In_2O_3 dimers have an identical In_2O_3 epitaxial growth direction along their *z*-axis, and thus the heterojunction plane is parallel to the (100) and (010) faces of the UO_2 and In_2O_3 segments (Figure 4).

Under this dimer attachment orientation, the In_2O_3 segment epitaxially grows on the (200) and (020) faces of the UO_2 seeds,

dx.doi.org/10.1021/ja2023724 |*J. Am. Chem. Soc.* 2011, 133, 14327–14337

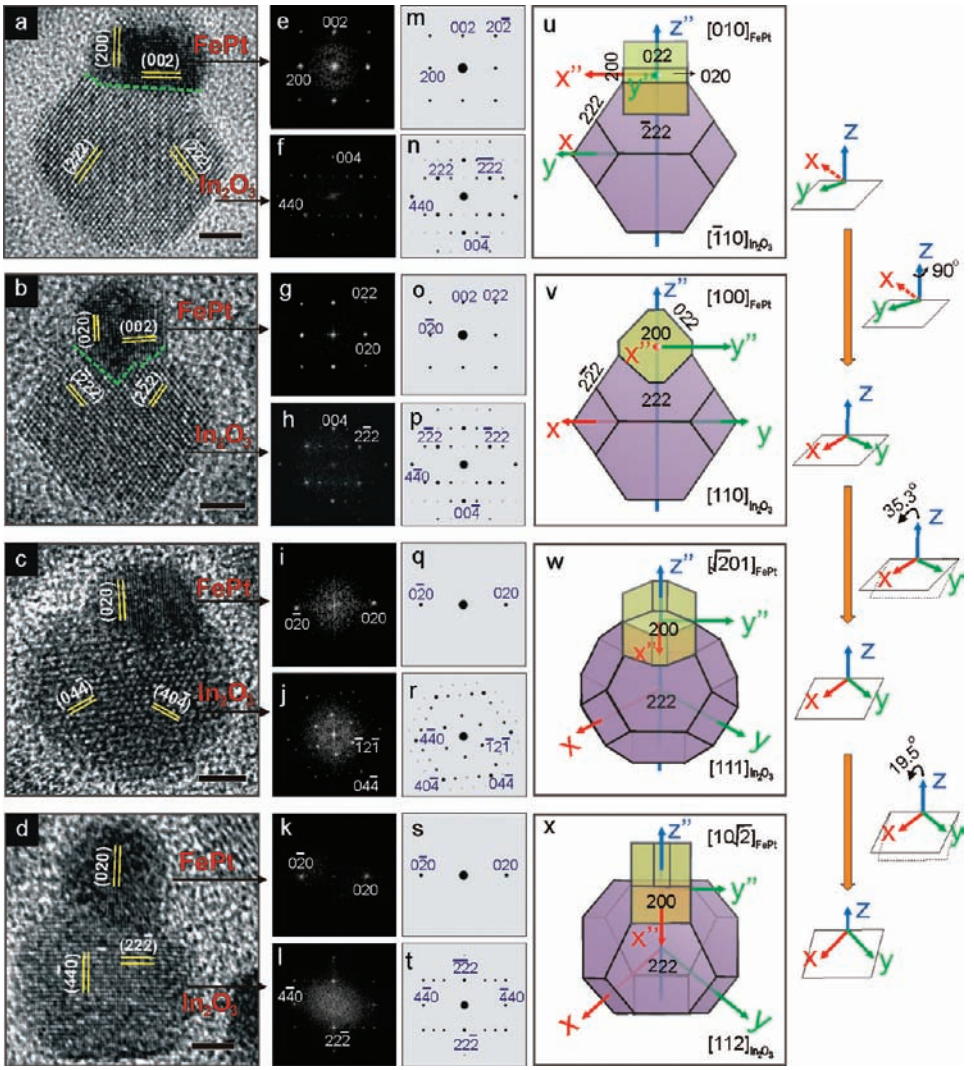

Figure 5. (a−d) HRTEM images of FePt/In_2O_3 hybrid nanocrystal at different orientations. Fast Fourier transform (FFT) patterns of the HRTEM images are shown in (e)−(l). The simulated electron diffraction patterns of differently oriented FePt/In_2O_3 hybrid nanocrystals are shown in (m)−(t) and are from the In_2O_3 side. Cartoons of an FePt/In_2O_3 hybrid nanocrystal at different orientations are shown in (u)−(x). The scale bars are 3 nm.

forming the (400) and (040) faces of its own crystal (In_2O_3), respectively. The *d*-spacing of {200} of UO_2 is 2.733 Å, 7.4% greater than that of {400} of In_2O_3 (2.529 Å), and this epitaxial growth should lead to lattice compression in the (200) and (020) faces of UO_2 segment and lattice expansion in the (400) and (040) faces of In_2O_3 segments. Therefore, this dimer attachment model is consistent with the results from XRD measurements (Figure 3 and Table S1). Although we cannot identify the exact chemical compositions across the dimer junction, it is still safe to conclude that the UO_2 lattice is compressed and the In_2O_3 lattice is expanded in the junction area.

Interestingly, the FFT images further reveal that the cubic bixbyite In_2O_3 exhibits more complicated lattice structure than that of the face-centered cubic UO_2. For example, in the [110] zone, the In_2O_3 segment exhibits additional {112} points as compared to that of the UO_2 segment (Figure 4f and g). Additional weak {002} and {420} points are shown along the [100] zone of the In_2O_3 segment (Figure 4d and e), and additional weak {244} points are shown along the [211] zone of the In_2O_3 segment (Figure 4h and i). Because ED simulations of bixbyite In_2O_3 nanoparticles by Crystalmaker software also show these weak diffraction spots (Figure 4k,m,o), the presence of these diffraction spots should not be generated from inherent nanostructural distortions in nanocrystals as observed by Caro et al.[69]

In addition, our HRTEM images show that, in a heterodimer, the UO_2 and In_2O_3 segments attach to each other through a large $(200)_{UO2}/(400)_{In2O3}$ junction (Figure 4), whose radius is about 5.1 nm. It is very clear that the area of $(200)_{UO2}$ in the heterojunction is much larger than the original area of the (200) facet on the spherical UO_2 nanocrystal seeds. This result suggests that the formation of the $(200)_{UO2}/(400)_{In2O3}$ heterojunction should be associated with surface rearrangement of UO_2 nanocrystal seeds, which could also be related to the size reduction of UO_2 seeds in the formation of UO_2/In_2O_3 dimers. Similar surface rearrangement of seed nanocrystals was more clearly observed in the formation of FePt/In_2O_3 dimers due to the rectangular shape of FePt seeds.

Unlike UO_2/In_2O_3 dimers, HRTEM studies show that the FePt and In_2O_3 segments in an FePt/In_2O_3 dimer are not in an identical zone axis (Figure 5). Four typical types of FePt/In_2O_3 dimer images were frequently observed under HRTEM

dx.doi.org/10.1021/ja2023724 |*J. Am. Chem. Soc.* 2011, 133, 14327–14337

(Figure 5a−d). When the In_2O_3 segment appears as the [$\bar{1}$10] or [110] zone image, the FePt segment exhibits the [010] or [100] zone image, respectively (Figure 5a and b). Interestingly, when the In_2O_3 segment image is in the [111] or [112] zone, the FePt segment does not have an on-axis cross-fringe image, but appears as single parallel (020) fringes (Figure 5c and d). In addition, the HRTEM zone-axis assignments are consistent with the corresponding FFT images. For example, the FFT image of the [111] In_2O_3 segment exhibits characteristic bixbyite {112} points (Figure 5j), and the FFT images of those off-axis images show only two dots (Figure 5i). Moreover, the HRTEM images further show that the (200) and (020) FePt fringes are parallel to the ($\bar{4}\bar{4}$0) and (4$\bar{4}$0) In_2O_3 fringes, respectively. However, these fringes are not visible across the heterojunction in the dimer.

The 3D structure simulation using Crystalmaker software suggests that the four types of HRTEM images should originate from heterodimers, of which the FePt and In_2O_3 segments have an identical geometric relationship (Figure 5u−x). In these dimers, the FePt and In_2O_3 segments share the same *z*-axis, but the *x*- and *y*-axes of the In_2O_3 segment are at an angle of 45° in relation to those of the FePt segment (Figure 5u). When rotating the dimer's *z*-axis by 90°, the FePt zone axis changes from [010] to [100], and the In_2O_3 zone axis changes from [$\bar{1}$10] to [110] (Figure 5u and v).

Tilting the dimer's *z*-axis out of the substrate plane at an angle of 35.3° or 19.5° changes the In_2O_3 zone axis to [111] or [112] (Figure 5w and x), whereas the FePt segment does not exhibit on-axis cross-fringe images. To label the orientations of the FePt segment specifically, we herein introduce the concept of an unconventional Miller index, which allows the use of irrational numbers. Accordingly, the zone axes of FePt are [$\sqrt{2}$01] and [10$\sqrt{2}$] when In_2O_3 exhibits the [111] and [112] zone images, respectively. Importantly, this unconventional index is valid in all of the existing crystallography formulas and should be very useful for analyzing the geometric relationships in different segments of heterogeneous nanomaterials. For example, one can easily calculate the orientation of the FePt segment using a conventional formula for cubic crystals:

$$\cos\theta = \frac{h_1 \times h_2 + k_1 \times k_2 + l_1 \times l_2}{\sqrt{h_1^2 + k_1^2 + l_1^2} \times \sqrt{h_2^2 + k_2^2 + l_2^2}}$$

Together, the results from HRTEM, FFT analysis, and structural simulations strongly suggest that the In_2O_3 attachment is along the *z*-axis direction of FePt seeds, whereas their *x*- and *y*-axes turn 45° from those of the FePt seeds. HRTEM images of FePt/In_2O_3 dimers show that the FePt segment has a shape of truncated rectangular prisms with exposed {110} faces (Figure 5 and Scheme 1). Evidently, in the [100] zone image, the FePt segment inserts into the In_2O_3 segment via a partially truncated "V" shaped structure, whereas the heterojunction appears to be a straight line when the FePt segment is in the [010] zone (Figure 5a,b,u,v, and Scheme 1). The "V" shaped structure in the heterojuction corresponds to the (2$\bar{2}$2) and ($\bar{2}$22) faces in the In_2O_3 and the (10$\bar{1}$) and ($\bar{1}$01) faces in the FePt seed, respectively. The partially truncated "V" is caused by the angle mismatch between those faces. Rotating the dimer's *z*-axis by 90° (FePt zone axis from [100] to [010]) hides the "V" shaped interface and results in a straight line (Scheme 1). In this case, the *d*-spacing of the In_2O_3 {222} is 7.7% larger than that of the FePt {110}. Therefore, the growth of In_2O_3 can lead to expansion of the FePt lattice and compression of the In_2O_3 lattice; this consequence is in full agreement with the XRD measurement results (Figure 3 and Table S1). In addition, this epitaxial growth configuration indicates that the surface of the FePt seeds (Figure S2) should be rearranged because the rectangular prisms are enclosed by only six {100} faces.

Scheme 1. Schematic Illustration of the Epitaxial Growth Configuration of an FePt/In_2O_3 Heterodimer[a]

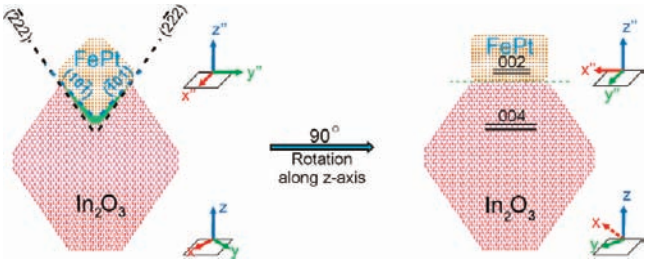

[a] The green area highlights the heterojunction in this dimer.

Another possible model for the In_2O_3/FePt dimer is that the (4$\bar{4}$0) and ($\bar{4}$40) faces of In_2O_3 grow epitaxially onto the (200) and (020) face of FePt seeds. The lattice mismatch of this attachment configuration is only 6.2% between these faces: the *d*-spacing of In_2O_3 {440} is 0.1789 nm, and the *d*-spacing of FePt {200} is 0.1907 nm. However, in this configuration, the interface should be a straight line instead of a "V" shape. Also, the *d*-spacing of FePt {200} is larger than that of In_2O_3 {440}. The epitaxial growth of In_2O_3 should lead to the compression of the FePt lattice and the expansion of the In_2O_3 lattice. These consequences contradict the experimental results of our XRD measurements (Figure 3 and Table S1) and HRTEM observations.

GENERAL DISCUSSION

On the basis of the results from this work, as well as those from existing literature, we have drawn general insights into the colloidal synthesis of heterodimer nanocrystals. We first discuss the principles behind the epitaxial growth orientation in heterodimers. We then discuss the growth models for the formation of colloidal heterodimers and the general criteria for their synthesis.

It is a major challenge to predict the crystallographic orientation of epitaxial growth in the formation of colloidal heterodimers. Current knowledge used to qualitatively explain epitaxial growth in heterodimers is adapted from studies of thin-film epitaxial growth. The explanations for epitaxial growth are primarily based on the lattice matching criterion in either simple unit cells or superlattice unit cells.[65] In thin-film epitaxial growth, lattice matching in simple unit cells is the criterion when the epitaxial material and substrate exhibit similar lattice constants, crystal structures, and nature of chemical bonds.[65] When at least one of these parameters in the epitaxial material differs significantly from those of the substrate (e.g., Si (111) on Al_2O_3 (101) and CdTe (111) on GaAs (100)), lattice mismatch in superlattice unit cells is the suitable criterion to determine epitaxial growth.[65] The theory of lattice matching in superlattice unit cells was developed by Zur and McGill in 1984.[70] It is very close to the Coincidence Site Lattice Theory,[71,72] which is typically used to explain the lattice grain boundary phenomena within identical materials.

In contrast to the case of thin-film epitaxial growth, multiple growth orientations are available for colloidal particle growth. Lattice matching criteria in either simple unit cells or superlattice

Scheme 2. Schematic Illustrations of the Preferred Bonding Directions in the Growth of Dimers[a]

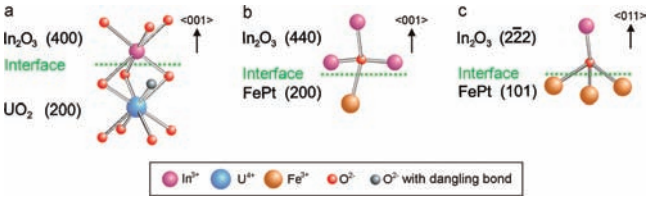

[a] (a) The (400) face of In_2O_3 on the (200) face of UO_2 along the ⟨001⟩ axis in the case of UO_2/In_2O_3 dimers. The bonding directions in the case of FePt/In_2O_3 dimers: (b) the (440) face of In_2O_3 on the (200) face of FePt, and (c) the (222) face of In_2O_3 on the (101) face of FePt.

unit cells cannot provide a priori solutions to the epitaxial growth orientation in colloidal heterodimers. In UO_2/In_2O_3 dimers, for example, many lattice matching pairs in the two materials have an identical lattice mismatch value (e.g., UO_2 (200) and In_2O_3 (400), UO_2 (220) and In_2O_3 (440), and UO_2 (111) and In_2O_3 (222)). Why is the UO_2 (200)/In_2O_3 (400) pair favorable over the others? In FePt/In_2O_3 dimers, the matching pair of FePt (200) and In_2O_3 (440) has a preface angle match and a smaller lattice match than the pair of FePt (110) and In_2O_3 (222), which has a large angle mismatch. Why is the second pair more favorable than the better matched FePt (200)/In_2O_3 (440) pair?

To answer these fundamental questions, we qualitatively analyzed the bonding energy difference between these lattice matching pairs. In a bixbyite In_2O_3 crystal, indium ions have a coordination number of six, and oxygen ions have a coordination number of four. Indium ions have a maximum bond number of three in both directions of the ⟨001⟩ axis, whereas oxygen ions have a maximum bond number of three in one direction of the ⟨011⟩ axis (Scheme 2). On the basis of bonding numbers, we can qualitatively estimate bonding energy for the epitaxial growth of In_2O_3. It is obvious that the epitaxial growth of indium along the ⟨001⟩ axis (i.e., epitaxial growth of In_2O_3 (400) on the UO_2 (200) face) can result in the highest bonding energy because of the triple bond of indium, which perfectly agrees with the experimental results.

This bonding energy criterion can also explain In_2O_3 epitaxial growth on FePt seeds. In this case, because of the weak metallic bonding nature between indium and the FePt lattice, the attachment of indium atoms at the first layer of epitaxial growth on FePt is not energetically favored, and therefore oxygen ions should be the first atomic layer of epitaxial growth. For the growth of oxygen ions, the ⟨011⟩ axis is the energy favored growth direction because of triple bonding (Scheme 2). In other words, In_2O_3 growth should start from its ($2\bar{2}2$) face on the substrate of the FePt (110) face, which is consistent with our XRD and TEM analyses.

In addition, the bonding energy criterion is also consistent with our experimental results that significant surface atomic rearrangement took place in the formation of both types of dimers. Spherical UO_2 seed nanocrystals merged as partial spheres in UO_2/In_2O_3 dimers for increasing available areas on the (100) and (010) faces for the attachment of In_2O_3 segment in a 3-fold coordination manner (Figure 4). In FePt/In_2O_3 dimers, the growth of In_2O_3 segment was not on the original surface of the rectangular FePt nanoprism seeds that are enclosed by the planes of {200}, but instead took place on the newly formed {220} faces through surface atomic arrangement, which allows for a strong triple-bond attachment of the first atomic layer of In_2O_3 (Figure 5 and Scheme 1).

Taken together, these results suggest that the affinity of the first atomic monolayer of an EP material to its seed nanocrystals plays a major role in determining the crystallographic orientation of the heterogeneous attachment. In other words, instead of growth on the facet of the nanocrystal seeds where less lattice mismatch exists, the growth of an EP material often takes place on the crystal facets where the first atomic monolayer of the EP material has the strongest affinity for the nanocrystal seeds.

To the best of our knowledge, this finding is consistent with the HRTEM observations of nearly all of the existing colloidal hybrid nanostructures in literature thus far. For instance, in Fe_2O_3/CdS hybrid nanoparticles, the epitaxial growth of zinc blende CdS starts from its (111) face on the Fe_2O_3 (111) face and is consistent with where cadmium or sulfur ions exhibit triple bonds in this crystal direction.[20] In the case of Au/Fe_3O_4 hybrid nanocrystals, the growth of the (111) Fe_3O_4 EP-layer on gold (111) accords with where oxygen ions exhibit triplet bonds in this orientation.[19] In addition, for gold growth onto spherical wurtzite CdSe nanocrystals, the gold attachment is on the CdSe (0001) face.[15] This face exhibits the highest density of selenium ions among all of the CdSe crystal faces, which should result in the highest affinity for the growth of gold atoms.

In short, our results, together with those from literature, are consistent with an empirical law that governs the formation of colloidal hybrid nanocrystals: the epitaxial attachment of an EP material onto a seed nanocrystal often occurs at the crystal facets where the first atomic monolayer of this EP material has the strongest affinity. Moreover, this empirical law applies to hybrid nanocrystals made from nonisotropic seeds, such as Au−CdSe−Au nanodumbbell and CdSe rod−Au (or Co) dimers.[11,15,47,48] In these cases, the epitaxial growth of Au (or Co) preferentially begins at the tips of CdSe rods, where selenium ions exist at their highest density, and thus have a large bonding affinity for Au (or Co) atoms.

We propose that this empirical law is a consequence of the competition between the multiple kinetic processes occurring in formation of colloidal hybrid nanocrystals (Scheme 3). These processes include (1) nonfacet selective attachment of the monomers of the EP material onto seed nanocrystals, which is determined by random collisions between a monomer and a seed nanocrystal; (2) detachment of these monomers from the surface of the seed nanocrystals, in which weaker-bonded monomers leave the nanocrystal surface, whereas the stronger bonded ones can stay as nuclei for further growth of the EP materials; (3) growth of the EP materials onto the nuclei on the surface of seed nanocrystals; (4) intraparticle ripening of the islands of EP materials on the surface of a single seed nanocrystal, which can merge two or more islands of EP materials into a single one; and (5) interparticle ripening of the EP material on the seed surface and free nanocrystals formed via new nucleation of the EP material, which can lead to the size reduction or even complete loss of the segment of the EP material attached onto seed nanocrystals (Scheme 3).

Under kinetic growth model, the resulting heterodimer nanocrystals are "survivors" of the following detachment kinetic processes (Scheme 3). First, monomers of EP material can directly detach from the surface of seeds due to their weak affinity, and the surviving ones become nuclei for further growth of EP materials. Second, the growth of EP materials can generate

Scheme 3. Kinetic Growth Model of Heterodimer Nanocrystals

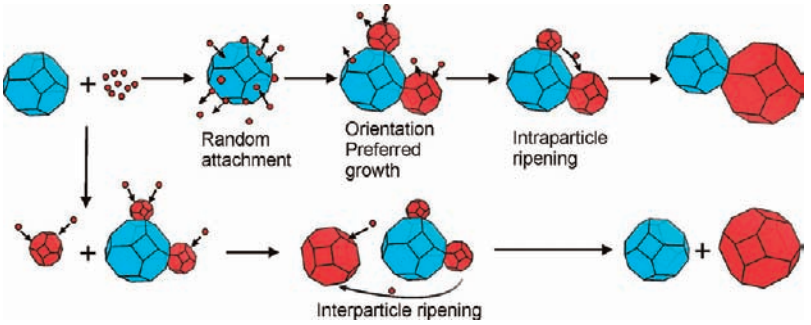

lattice strains at the heterojunction, and thus further result in the detachment of EP material segments, in which the first epitaxial layer has relatively weaker affinity to the seed surface (please note that similar strain-induced heterodimer detachment has been well-documented by Sun et al. in their study of Fe_2O_3/Au dimers[73]).

Third, intraparticle ripening is another kinetic process that leads to the detachment of the EP materials. In this detachment process, the islands of EP material, with small size and/or relatively weak-bonded first epitaxial atomic layer, are polished from seed surface. Intraparticle ripening phenomenon was discovered by Banin et al. in the synthesis of CdSe−gold dimers.[11,15] Here, we have also observed trimers (i.e., FePt nanocrystal with two In_2O_3 segments) in the synthesis of FePt/In_2O_3 hybrid nanocrystals (Figure S3 in the Supporting Information). Last, interparticle ripening also leads to the detachment of the EP material from seed nanocrystals (Scheme 2, Figure S1).

After these detachment processes, the survived heterodimers should exhibit a structure, in which the EP material segment is attached in the crystallographic orientation that allows the first atomic layer of the segment to have the strongest affinity to the surface of seed nanocrystals. Therefore, we can see that the empirical law described herein is just a "selection rule" for kinetic evolution during the formation of colloidal heterodimers!

It is worth noting that the activation energy barrier heights of these kinetic processes may play roles in the attachment of EP materials during the formation of hybrid nanocrystals. In the case when the kinetic energy barrier of one (or more) of these processes is substantially high, we could expect that the growth of EP materials is in crystal orientations more than the one predicted by the empirical law. For example, hybrid nanocrystals can form with multiple heterojunctions, such as Fe_3O_4/CdS hybrid nanocrystals made by Shim et al.[20] In CdSe/CdTe nanorod heterostructures, the CdTe attachment onto the tips of CdSe nanorods is the crystallographic orientation that CdTe has strongest affinity. Shim et al. observed that CdTe segments attached onto both the tips and the sides of the CdSe nanorods forming curved CdSe/CdTe nanorod heterostructures,[74] which is consistent with the kinetic mechanism.

Moreover, interparticle ripening is a kinetic process, which has not been well studied previously, with the exception of the observation herein: new nucleation and the subsequent growth of In_2O_3 free nanocrystals led to the complete loss of In_2O_3 segments from UO_2/In_2O_3 dimers and also the size reduction of the UO_2 nanocrystals (Figure S1). Interparticle ripening should also exhibit a kinetic energy barrier. When this energy barrier is substantially high, heterodimers can still survive this ripening kinetic competition even in the presence of new nucleation of the EP materials. For example, Parak and Manna et al. have demonstrated a successful synthesis of PbSe/CdSe/PbSe nanodumbbells in the presence of nucleation of PbSe nanocrystals.[17]

CONCLUSION

We have demonstrated a colloidal synthesis of high-quality UO_2/In_2O_3 and FePt/In_2O_3 dimer nanocrystals. The resulting nanocrystals were characterized using XRD, EDS, TEM, STEM, and HRTEM. The results from XRD measurements suggest that lattice strains exist in both of these dimer nanocrystals. The lattice of In_2O_3 expands, but the UO_2 lattice gets compressed in UO_2/In_2O_3 dimers. FePt/In_2O_3 dimers exhibit compressed In_2O_3 lattices and expanded lattices in FePt seeds. Using XRD, HRTEM, and nanocrystal structure simulations, we have identified the crystallographic orientations of the attachment of the two segments in these two types of dimers. An unconventional Miller index was introduced to describe the crystallographic orientation of these heterodimer nanocrystals.

On the basis of the results herein as well as those from existing literature, we propose an empirical law for the determination of the attachment orientation in heterodimers: the growth of an EP material onto a seed nanocrystal often takes place at the crystal facets, in which the first atomic monolayer of the EP material has the strongest affinity to the seed nanocrystals. In the end, we anticipate that the new findings can be useful for creating an a priori design of synthesis methods for making colloidal hybrid nanocrystals of new compositions in complex structures for new demands in technological development areas such as biomedical diagnosis, disease control and prevention, solar energy conversion, and spintronics.[43,75]

ASSOCIATED CONTENT

Supporting Information. Detailed synthetic procedures, TEM images, and XRD data. This material is available free of charge via the Internet at http://pubs.acs.org.

AUTHOR INFORMATION

Corresponding Author
cao@chem.ufl.edu

ACKNOWLEDGMENT

We thank the Major Analytical Instrumentation Center (MAIC) at the University of Florida for TEM and XRD usage.

Y.C.C. acknowledges the NSF (DMR-0645520 Career Award) and the ONR (N00014-09-1-0441).

REFERENCES

(1) Costi, R.; Cohen, G.; Salant, A.; Rabani, E.; Banin, U. *Nano Lett.* **2009**, *9*, 2031–2039.
(2) Figuerola, A.; Fiore, A.; Di Corato, R.; Falqui, A.; Giannini, C.; Micotti, E.; Lascialfari, A.; Corti, M.; Cingolani, R.; Pellegrino, T.; Cozzoli, P. D.; Manna, L. *J. Am. Chem. Soc.* **2008**, *130*, 1477–1487.
(3) Teranishi, T.; Wachi, A.; Kanehara, M.; Shoji, T.; Sakuma, N.; Nakaya, M. *J. Am. Chem. Soc.* **2008**, *130*, 4210–4211.
(4) Gu, H.; Zheng, R.; Zhang, X.; Xu, B. *J. Am. Chem. Soc.* **2004**, *126*, 5664–5664.
(5) Wang, C.; Daimon, H.; Sun, S. *Nano Lett.* **2009**, *9*, 1493–1496.
(6) Ronny, C.; Aaron, E. S.; Uri, B. *Angew. Chem., Int. Ed.* **2010**, *49*, 4878–4897.
(7) Cozzoli, P. D.; Pellegrino, T.; Manna, L. *Chem. Soc. Rev.* **2006**, *35*, 1195–1208.
(8) Carbonea, L.; Cozzoli, P. D. *Nano Today* **2010**, *5*, 449–493.
(9) Casavola, M.; Buonsanti, R.; Caputo, G.; Cozzoli, P. D. *Eur. J. Inorg. Chem.* **2008**, *6*, 837–854.
(10) Milliron, D. J.; Hughes, S. M.; Cui, Y.; Manna, L.; Li, J.; Wang, L.-W.; Paul Alivisatos, A. *Nature* **2004**, *430*, 190–195.
(11) Mokari, T.; Rothenberg, E.; Popov, I.; Costi, R.; Banin, U. *Science* **2004**, *304*, 1787–1790.
(12) Buonsanti, R.; Grillo, V.; Carlino, E.; Giannini, C.; Kipp, T.; Cingolani, R.; Cozzoli, P. D. *J. Am. Chem. Soc.* **2008**, *130*, 11223–11233.
(13) Talapin, D. V.; Lee, J.-S.; Kovalenko, M. V.; Shevchenko, E. V. *Chem. Rev.* **2009**, *110*, 389–458.
(14) Claudia, P.; Andreas, K.; Horst, W. *Angew. Chem., Int. Ed.* **2004**, *43*, 4774–4777.
(15) Mokari, T.; Sztrum, C. G.; Salant, A.; Rabani, E.; Banin, U. *Nat. Mater.* **2005**, *4*, 855–863.
(16) Halpert, J. E.; Porter, V. J.; Zimmer, J. P.; Bawendi, M. G. *J. Am. Chem. Soc.* **2006**, *128*, 12590–12591.
(17) Kudera, S.; Carbone, L.; Casula, M. F.; Cingolani, R.; Falqui, A.; Snoeck, E.; Parak, W. J.; Manna, L. *Nano Lett.* **2005**, *5*, 445–449.
(18) Spoerke, E. D.; Lloyd, M. T.; Lee, Y.-j.; Lambert, T. N.; McKenzie, B. B.; Jiang, Y.-B.; Olson, D. C.; Sounart, T. L.; Hsu, J. W. P.; Voigt, J. A. *J. Phys. Chem. C* **2009**, *113*, 16329–16336.
(19) Yu, H.; Chen, M.; Rice, P. M.; Wang, S. X.; White, R. L.; Sun, S. *Nano Lett.* **2005**, *5*, 379–382.
(20) Kwon, K.-W.; Shim, M. *J. Am. Chem. Soc.* **2005**, *127*, 10269–10275.
(21) Lim, B.; Jiang, M.; Camargo, P. H. C.; Cho, E. C.; Tao, J.; Lu, X.; Zhu, Y.; Xia, Y. *Science* **2009**, *324*, 1302–1305.
(22) Habas, S. E.; Lee, H.; Radmilovic, V.; Somorjai, G. A.; Yang, P. *Nat. Mater.* **2007**, *6*, 692–697.
(23) Habas, S. E.; Yang, P.; Mokari, T. *J. Am. Chem. Soc.* **2008**, *130*, 3294–3295.
(24) Shi, W.; Zeng, H.; Sahoo, Y.; Ohulchanskyy, T. Y.; Ding, Y.; Wang, Z. L.; Swihart, M.; Prasad, P. N. *Nano Lett.* **2006**, *6*, 875–881.
(25) Gu, H.; Yang, Z.; Gao, J.; Chang, C. K.; Xu, B. *J. Am. Chem. Soc.* **2004**, *127*, 34–35.
(26) Robinson, R. D.; Sadtler, B.; Demchenko, D. O.; Erdonmez, C. K.; Wang, L.-W.; Alivisatos, A. P. *Science* **2007**, *317*, 355–358.
(27) Zhuang, J.; Shaller, A. D.; Lynch, J.; Wu, H.; Chen, O.; Li, A. D. Q.; Cao, Y. C. *J. Am. Chem. Soc.* **2009**, *131*, 6084–6085.
(28) Dawson, A.; Kamat, P. V. *J. Phys. Chem. B* **2001**, *105*, 960–966.
(29) Subramanian, V.; Wolf, E. E.; Kamat, P. V. *J. Phys. Chem. B* **2003**, *107*, 7479–7485.
(30) Wood, A.; Giersig, M.; Mulvaney, P. *J. Phys. Chem. B* **2001**, *105*, 8810–8815.
(31) Buonsanti, R.; Snoeck, E.; Giannini, C.; Gozzo, F.; Garcia-Hernandez, M.; Garcia, M. A.; Cingolani, R.; Cozzoli, P. D. *Phys. Chem. Chem. Phys.* **2009**, *11*, 3680–3691.
(32) Gao, J.; Zhang, W.; Huang, P.; Zhang, B.; Zhang, X.; Xu, B. *J. Am. Chem. Soc.* **2008**, *130*, 3710–3711.
(33) Buonsanti, R.; Grillo, V.; Carlino, E.; Giannini, C.; Curri, M. L.; Innocenti, C.; Sangregorio, C.; Achterhold, K.; Parak, F. G. n.; Agostiano, A.; Cozzoli, P. D. *J. Am. Chem. Soc.* **2006**, *128*, 16953–16970.
(34) Murphy, C. J.; Sau, T. K.; Gole, A. M.; Orendorff, C. J.; Gao, J.; Gou, L.; Hunyadi, S. E.; Li, T. *J. Phys. Chem. B* **2005**, *109*, 13857–13870.
(35) Yang, J.; Elim, H. I.; Zhang, Q.; Lee, J. Y.; Ji, W. *J. Am. Chem. Soc.* **2006**, *128*, 11921–11926.
(36) Murphy, C. J.; Jana, N. R. *Adv. Mater.* **2002**, *14*, 80–82.
(37) Gao, J.; Zhang, B.; Gao, Y.; Pan, Y.; Zhang, X.; Xu, B. *J. Am. Chem. Soc.* **2007**, *129*, 11928–11935.
(38) Cheng, C.; Yu, K. F.; Cai, Y.; Fung, K. K.; Wang, N. *J. Phys. Chem. C* **2007**, *111*, 16712–16716.
(39) Fabienne, W.; Katerina, S.; Andrea, F.; Marc, R.; Etienne, S.; Bruno, C. *Angew. Chem., Int. Ed.* **2007**, *46*, 7079–7081.
(40) Casavola, M.; Grillo, V.; Carlino, E.; Giannini, C.; Gozzo, F.; Fernandez Pinel, E.; Garcia, M. A.; Manna, L.; Cingolani, R.; Cozzoli, P. D. *Nano Lett.* **2007**, *7*, 1386–1395.
(41) Wang, Z.; Li, Z.-x.; Liu, Z. *J. Phys. Chem. C* **2009**, *113*, 3899–3902.
(42) Battie, Y.; Destouches, N.; Bois, L.; Chassagneux, F.; Tishchenko, A.; Parola, S. p.; Boukenter, A. *J. Phys. Chem. C* **2010**, *114*, 8679–8687.
(43) Deka, S.; Falqui, A.; Bertoni, G.; Sangregorio, C.; Poneti, G.; Morello, G.; Giorgi, M. D.; Giannini, C.; Cingolani, R.; Manna, L.; Cozzoli, P. D. *J. Am. Chem. Soc.* **2009**, *131*, 12817–12828.
(44) Casavola, M.; Falqui, A.; Garcia, M. A.; Garcia-Hernandez, M.; Giannini, C.; Cingolani, R.; Cozzoli, P. D. *Nano Lett.* **2009**, *9*, 366–376.
(45) Pellegrino, T.; Fiore, A.; Carlino, E.; Giannini, C.; Cozzoli, P. D.; Ciccarella, G.; Respaud, M.; Palmirotta, L.; Cingolani, R.; Manna, L. *J. Am. Chem. Soc.* **2006**, *128*, 6690–6698.
(46) Buonsanti, R.; Grillo, V.; Carlino, E.; Giannini, C.; Gozzo, F.; Garcia-Hernandez, M.; Garcia, M. A.; Cingolani, R.; Cozzoli, P. D. *J. Am. Chem. Soc.* **2010**, *132*, 2437–2464.
(47) Menagen, G.; Macdonald, J. E.; Shemesh, Y.; Popov, I.; Banin, U. *J. Am. Chem. Soc.* **2009**, *131*, 17406–17411.
(48) Saunders, A. E.; Popov, I.; Banin, U. *J. Phys. Chem. B* **2006**, *110*, 25421–25429.
(49) Lee, J.-S.; Bodnarchuk, M. I.; Shevchenko, E. V.; Talapin, D. V. *J. Am. Chem. Soc.* **2010**, *132*, 6382–6391.
(50) Jérôme, M.; Asaf, S.; Andrea, F.; Marc, R.; Ehud, S.; Uri, B.; Katerina, S.; Bruno, C. *Angew. Chem., Int. Ed.* **2009**, *48*, 1814–1817.
(51) Lin, Z.-H.; Lin, Y.-W.; Lee, K.-H.; Chang, H.-T. *J. Mater. Chem.* **2008**, *18*, 2569–2572.
(52) Vinod, T. P.; Yang, M.; Kim, J.; Kotov, N. A. *Langmuir* **2009**, *25*, 13545–13550.
(53) Sun, S.; Murray, C. B.; Weller, D.; Folks, L.; Moser, A. *Science* **2002**, *287*, 1989–1992.
(54) Marezio, M. *Acta Crystallogr.* **1966**, *20*, 723–728.
(55) Ruello, P.; Petot-Ervas, G.; Petot, C.; Desgranges, L. *J. Am. Ceram. Soc.* **2005**, *88*, 604–611.
(56) Chen, W.; Kim, J.; Sun, S.; Chen, S. *J. Phys. Chem. C* **2008**, *112*, 3891–3898.
(57) Chen, M.; Kim, J.; Liu, J. P.; Fan, H.; Sun, S. *J. Am. Chem. Soc.* **2006**, *128*, 7132–7133.
(58) Elkins, K.; Li, D.; Poudyal, N.; Nandwana, V.; Jin, Z.; Chen, K.; Liu, J. P. L. *J. Phys. D: Appl. Phys.* **2006**, 2306–2309.
(59) Liu, Q.; Lu, W.; Ma, A.; Tang, J.; Lin, J.; Fang, J. *J. Am. Chem. Soc.* **2005**, *127*, 5276–5277.
(60) Zhang, D.; Liu, Z.; Li, C.; Tang, T.; Liu, X.; Han, S.; Lei, B.; Zhou, C. *Nano Lett.* **2004**, *4*, 1919–1924.
(61) Zhang, D.; Li, C.; Liu, X.; Han, S.; Tang, T.; Zhou, C. *Appl. Phys. Lett.* **2003**, *83*, 1845–1847.
(62) Gordon, R. G. *MRS Bull.* **2000**, *25*, 52–57.
(63) Gopchandran, K. G.; Joseph, B.; Abraham, J. T.; Koshy, P.; Vaidyan, V. K. *Vacuum* **1997**, *48*, 547–550.
(64) Utsunomiya, S.; Ewing, R. C. *Environ. Sci. Technol.* **2003**, *37*, 786–791.
(65) Herman, M. A.; Richter, W.; Siter, H. *Epitaxy: Physical Principles and Technical implementation*; Springer: Berlin, 2004.

(66) Smith, A. M.; Mohs, A. M.; Nie, S. *Nat. Nanotechnol.* **2009**, *4*, 56–63.
(67) Boresi, A. P.; Schmidt, R. J.; Sidebottom, O. M. *Advanced Mechanics of Materials*; John Wiley & Sons: New York, 1993.
(68) Lekhnitskii, S. *Theory of Elasticity of an Anisotropic Elastic Body*; Holden-Day Inc.: San Francisco, CA, 1963.
(69) Caro, L. D.; Carlino, E.; Caputo, G.; Cozzoli, P. D.; Giannini, C. *Nat. Nanotechnol.* **2010**, *5*, 360.
(70) Zur, A.; McGill, T. C. *J. Appl. Phys.* **1984**, 378–386.
(71) Bollmann, W. *Crystal Defects and Crystalline Interfaces*; Springer-Verlag: Berlin, 1970.
(72) Brokman, A.; Balluffi, R. W. *Acta Metall.* **1981**, *29*, 1703–1719.
(73) Wang, C.; Wei, Y.; Jiang, H.; Sun, S. *Nano Lett.* **2009**, *9*, 4544–4547.
(74) McDaniel, H.; Zou, J.-M.; Shim, M. *J. Am. Chem. Soc.* **2010**, *132*, 3286–3288.
(75) Bauer, C.; Boschloo, G.; Mukhtar, E.; Hagfeldt, A. *J. Phys. Chem. B* **2001**, *105*, 5585–5588.